

## Elucidating the roles of collision energy and photon momentum transfer in the formation of ultralong-range Rydberg molecules

C. Wang,<sup>1,2</sup> Y. Lu,<sup>1</sup> S. K. Kanungo,<sup>1</sup> F. B. Dunning<sup>1,2</sup>, T. C. Killian<sup>1,2</sup>, and S. Yoshida<sup>3</sup>

<sup>1</sup>*Department of Physics and Astronomy, Rice University, Houston, Texas 77005-1892, USA*

<sup>2</sup>*Smalley-Curl Institute, Rice University, Houston, Texas 77005-1892, USA*

<sup>3</sup>*Institute for Theoretical Physics, Vienna University of Technology, A-1040 Vienna, Austria, EU*



(Received 14 June 2024; accepted 13 August 2024; published 6 September 2024)

Spectroscopic measurements of the rotational distribution of  $^{84}\text{Sr}$  and  $^{86}\text{Sr}$   $5ns\ ^1S_0$  ultralong-range Rydberg molecular dimers created via photoassociation in a cold gas are reported. The dimers are produced by two-photon excitation via the  $5s5p\ ^1P_1$  intermediate state. The use of singlet states permits detailed study of the roles that the initial atom-atom interaction, photon momentum transfer during Rydberg excitation, and sample temperature play in determining the spectral line shape and final dimer rotational distribution. The results are in good agreement with the predictions of a model that includes these effects. The present work further highlights the sensitivity of ultralong-range Rydberg molecule formation to the state of the initial cold gas.

DOI: [10.1103/PhysRevA.110.032803](https://doi.org/10.1103/PhysRevA.110.032803)

### I. INTRODUCTION

Interest in ultralong-range Rydberg molecules (ULRRMs), which comprise a Rydberg atom in whose electron cloud are embedded one (or more) weakly bound ground-state atoms, has increased steadily over the years [1–5]. Such molecules, which represent a new molecular class, have provided a valuable microscale laboratory in which to study low-energy electron-atom scattering at energies not readily accessible using alternate techniques [6,7], have furnished a powerful probe of nonlocal spatial correlations in cold quantum gases [8,9], illuminating the important role played by quantum statistics, and have, through measurements of ULRRM formation in dense Bose-Einstein condensates, provided the opportunity to study many-body phenomena, such as the creation of Rydberg polarons [10–13].

ULRRMs are bound by scattering of the Rydberg electron from the ground-state atom which, as demonstrated in earlier studies, can frequently be described using a zero-range Fermi pseudopotential [14,15]. The resulting molecular Born-Oppenheimer potential can support multiple vibrational states. In the case of strontium  $ns$  Rydberg states, the ground  $v = 0$  vibrational state is of particular interest because it is strongly localized near the outer classical turning point at an internuclear separation,  $R_n \sim 1.8(n - \delta)^2 a_0$ , where  $n$  is the principal quantum number,  $a_0$  is the Bohr radius, and  $\delta$  is the quantum defect.

The vibrational structure of ULRRMs has been examined in a number of earlier studies. Recent work, however, extended measurements to include the study of their rotational structure [15]. These studies employed  $^{86}\text{Sr}$   $5ns\ ^3S_1$  dimers because the scattering length for  $^{86}\text{Sr}$ - $^{86}\text{Sr}$  collisions is unusually large,  $a_s = 811a_0$ , and is comparable in size to the internuclear separation for  $v = 0$  strontium ULRRM dimers with values of  $n \sim 25$ . Since the value of  $a_s$  defines the position of a node in the atom-atom scattering wave function, the probability of finding an atom pair with initial separations close to this value is reduced. Thus, for values of  $n$  near

25, the Franck-Condon overlap between the initial scattering state and the final ( $v = 0$ ) molecular state is reduced, thereby suppressing dimer formation via the  $s$ -wave channel. This, in turn, allows the effects of higher-partial-wave scattering, which can lead to the creation of rotationally excited dimers, to be more visible. Furthermore, in the formation of ULRRM dimers only one atom in the initial ground-state pair acquires photon momentum through its excitation which, given the large size of the product dimer, can lead to significant angular momentum transfer to the atom pair. The earlier experimental results for  $^3S_1$  dimers, however, were not in good agreement with the predictions of a theoretical model which incorporated the effects of both the scattering length and the recoil photon momentum. The interaction of the electron spins with the molecular rotational motion was estimated to be small and was neglected. In this paper photoassociation spectra for Rydberg dimers created using singlet  $5ns\ ^1S_0$  Rydberg states are analyzed to examine if the discrepancies observed in the previous study are peculiar to strontium triplet Rydberg states.

The  $^{86}\text{Sr}$   $5ns\ ^3S_1$  ( $m = +1$ ) Rydberg dimers employed in the earlier experiments [15] were created by two-photon excitation via the intermediate  $5s5p\ ^3P_1$  state using lasers operating at 689 and 320 nm. The role of photon momentum transfer could not be clearly identified because, even when the laser beams counterpropagate, significant momentum transfer occurs. Here we remove this limitation by studying the formation of  $5ns\ ^1S_0$  dimers created by two-photon excitation via the intermediate  $5s5p\ ^1P_1$  state, which requires lasers operating at 461 and 413 nm. Thus, if the lasers counterpropagate, the net photon momentum transfer is very small, thereby providing a benchmark against which to identify the effects of photon momentum transfer. To examine the effects of photon momentum transfer, copropagating laser beams are employed.

The effects of the initial atom-atom interaction are explored through comparative measurements using  $^{84}\text{Sr}$  for which the  $s$ -wave scattering length,  $a_s = 123a_0$ , is much less than that for  $^{86}\text{Sr}$ .

The measurements are compared with the results of model calculations that include the effects of both the initial atom-atom interaction and of photon momentum transfer. The theoretical predictions are in good agreement with experiment and highlight the important role that these factors, together with the initial cold gas temperature, play in determining the rotational distribution of the product ULRRMs.

## II. EXPERIMENTAL METHOD

The experimental methods are described in detail elsewhere [16–18]. Briefly, strontium atoms are laser-cooled to a few microkelvin and loaded into a “pancake”-shaped optical dipole trap (ODT) formed from two crossed elliptical 1064 nm laser beams. Evaporative cooling is used to further lower and control the atom temperature. The Rydberg molecules are created by two-photon excitation via the intermediate  $5s5p\ ^1P_1$  state. The necessary radiation at 461 nm ( $5s^2\ ^1S_0 \rightarrow 5s5p\ ^1P_1$ ) and 413 nm ( $5s5p\ ^1P_1 \rightarrow 5sns\ ^1S_0$ ) is provided by frequency-doubled diode laser systems that are stabilized to high-finesse ultralow-expansion optical cavities. To limit trap loss and heating from photon scattering, the 461 nm laser was blue-detuned by  $\sim 18$  GHz. The photoexcitation lasers are typically applied for  $\sim 20$   $\mu$ s. Whereas the laser linewidths are small, typically a few kHz, the effective instrumental linewidth, measured by observing the excitation of atomic Rydberg states using counterpropagating beams, is larger  $\sim 50$  kHz and is limited by transform broadening associated with the 20  $\mu$ s laser pulse width (when using counterpropagating laser beams Doppler broadening is minimal.) It is, however, a significant improvement in linewidth as compared to that in earlier measurements,  $\sim 120$ – $140$  kHz [15], and is sufficiently narrow as to allow detailed spectroscopic studies of molecular photoassociation.

The ODT was loaded with  $\sim 5$ – $10 \times 10^5$  atoms, resulting in trap densities of up to  $\sim 1 \times 10^{13}$   $\text{cm}^{-3}$ . The final atom number, and temperature, were determined through absorption imaging on the  $5s^2\ ^1S_0 \rightarrow 5s5p\ ^1P_1$  transition following release of the atoms from the ODT and a fall time of  $\sim 20$  ms.

The number of Rydberg molecules produced is determined through ionization in a pulsed electric field [19,20]. The resulting electrons are directed to a dual-microchannel plate for detection and counted. Experimental limitations on the size of the ionizing field that could be generated in the experimental volume limited measurements to states with  $n \geq 29$ . Excitation rates were kept low, typically  $\lesssim 0.3$  per experimental cycle, to minimize possible effects due to Rydberg-Rydberg interactions. The need to maintain a constant sample temperature and density during a set of measurements limited the number of experimental cycles that could be undertaken using a single cold-atom sample to  $\sim 200$ .

## III. THEORETICAL ANALYSIS

The present results are interpreted using a theoretical model that has been described in detail previously [15] and which includes the effects of ground-state atom-atom interactions in the initial scattering channel, together with the recoil momentum associated with photon momentum transfer.

Since a Rydberg dimer is formed by a weak perturbation to isolated atoms, the two atoms in the molecule can be treated as composite, identical bosonic particles as they are in the initial scattering state. Thus the Hamiltonian of the interacting atoms is invariant with an exchange of both electron and ion coordinates simultaneously and the wave functions are symmetric with respect to the overall exchange. However, for an initial scattering state in which both atoms are in the same electronic state (the  $5s^2$  ground state), the wave function becomes symmetric with respect to only the ion coordinates. When a partial-wave representation  $|k, N', M'_N\rangle$  is adopted for the relative motion of the colliding pair, where  $N'$  is the rotational quantum number,  $M'_N$  its projection on the quantization axis, and  $\hbar k$  is the relative momentum, only even partial waves are allowed for the initial scattering state. Thus, when the effects of recoil photon momentum are negligible, only even,  $N = 0, 2, 4, \dots$ , rotational states of the Rydberg dimer can be created. Since the total orbital angular momentum of the valence electrons in strontium vanishes, the total mechanical angular momentum of the product dimer is completely characterized by the quantum numbers  $N$  and  $M_N$ . The transition amplitude is given by an inelastic form factor that may be written

$$F_{v,N,M_N}(k, N', M'_N) = \frac{1}{\sqrt{2}} \langle v, N, M_N | [e^{-i(\vec{\kappa}/2)\cdot\vec{R}} + (-1)^N e^{i(\vec{\kappa}/2)\cdot\vec{R}}] | k, N', M'_N \rangle, \quad (1)$$

where  $v$  denotes the final vibrational state and  $\vec{\kappa}$  is the sum of the wave vectors associated with the laser fields. Here we assume no mixing between vibrational and rotational levels for the ground vibrational level since the energy difference between the vibrational levels  $v = 0$  and  $1$  is typically much larger than the rotational energies. This form factor is similar to that used in molecular spectroscopy except that it includes the effects of photon recoil momentum. The form factor is evaluated using spherical representations of both the initial asymptotic scattering state of the atomic pair and the final state of the Rydberg molecule and hence the transition amplitude can be approximated by

$$F_{v,N,M_N}(k, N', M'_N) \propto j_\lambda(\kappa R_n/2) \tilde{j}_{N'}(\kappa R_n), \quad (2)$$

where  $\lambda \simeq |N - N'|$  is the change in rotational quantum number and

$$\tilde{j}_{N'}(\kappa R) = \begin{cases} \frac{\sin[k(R-a_s)]}{\kappa R}, & N' = 0, \\ j_{N'}(\kappa R), & N' > 0, \end{cases} \quad (3)$$

where  $j_{N'}(\kappa R)$  is the spherical Bessel function. This form factor resembles the Franck-Condon (FC) overlap between the initial scattering state and final molecular state. The Franck-Condon principle, however, argues that electronically and vibrationally excited states are formed by “vertical” transitions at a given internuclear separation and that rotational angular momentum will be conserved during photoassociation. The nondiagonal transitions with  $N - N' \neq 0$  seen here result from the interplay of photon momentum recoil and the large molecular size. The angular momentum transferred to the dimer,  $\sim \kappa R_n/2$ , when using counterpropagating beams,

$\sim 0.04$  a.u., is very much less than when using copropagating beams,  $\sim 0.9$  a.u..

The final excitation strength,  $f(\omega)$ , is obtained by averaging over the Boltzmann distribution of the relative momenta for atoms in the trap and the effective laser linewidths,

$$f(\omega) \propto \sqrt{\frac{2}{\pi}} \left( \frac{\hbar^2}{\mu k_B T} \right)^{3/2} \sum_{v,N,M_N} \int d\vec{k} k^2 e^{-\hbar^2 k^2 / (2\mu k_B T)} \times \sum_{N',M'_N} |F_{v,N,M_N}(k, N', M'_N)|^2 L_{v,N}(k, \omega), \quad (4)$$

where  $L_{v,N}$  is a normalized line-shape function which, for the present experimental data, can be well approximated by a distribution including the Doppler broadening induced by the center-of-mass momentum  $\hbar \vec{k}_{c.m.}$  of the dimer,

$$L_{v,N}(k, \omega) = \frac{1}{\pi} \left( \frac{\hbar^2}{2\pi M k_B T} \right)^{3/2} \int d\vec{k}_{c.m.} e^{-\hbar^2 k_{c.m.}^2 / (2M k_B T)} \times \frac{2\Gamma}{4[\omega - \hbar \vec{k} \cdot \vec{k}_{c.m.} / M + \hbar k^2 / (2\mu) - E_{v,N} / \hbar]^2 + \Gamma^2}, \quad (5)$$

where  $M$  is the total mass of the dimer and  $\mu = M/4$  the reduced mass,  $\hbar^2 k^2 / 2\mu$  the initial relative kinetic energy of the collision pair,  $\omega$  the two-photon detuning from atomic resonance for an atom at rest, and  $\Gamma$  the full width at half maximum (FWHM) of the effective instrumental linewidth. The peak position in Eq. (5) is determined by the initial relative kinetic energy of the collision pair, i.e.,  $E_{v,N} \simeq \hbar\omega + \hbar^2 k^2 / (2\mu)$  on resonance, and energy conservation during excitation. Note that thermal averaging, i.e., the convolution of Lorentzians with the Boltzmann distributions contained in Eqs. (4) and (5) leads to an increased linewidth and asymmetric non-Lorentzian overall line profiles [21] that can be calculated using the molecular binding energies  $E_{v,N}$  and the Franck-Condon overlap evaluated from the molecular Hamiltonian.

In order to extract rotational energies  $E_{v=0,N}$  and the contribution from each rotational level to the photoassociation spectra, the measured spectra are fit using the expression

$$f_{\text{fit}}(\omega) = \left( \frac{2\hbar^2}{\pi \mu k_B T} \right)^{3/2} \sum_N C_N \times \int d\vec{k} k^2 \frac{|\mathcal{F}_N(k)|^2 \Gamma e^{-\hbar^2 k^2 / (2\mu k_B T)}}{4[\omega + \hbar k^2 / (2\mu) - E_{v=0,N} / \hbar]^2 + \Gamma^2} \quad (6)$$

and the measured sample temperatures  $T$  while treating the effective linewidth  $\Gamma$ ,  $E_{v=0,N}$ , and weights,  $C_N$ , of the contributions from each rotational level as adjustable parameters. The Franck-Condon overlap is approximated using Eq. (2) as

$$\mathcal{F}_N(k) = \sum_{N'} j_\lambda(\kappa R_n / 2) \tilde{j}_{N'}(k R_n), \quad (7)$$

with  $\lambda = |N - N'| = 0$  for even  $N$  and 1 for odd  $N$ . In fitting the data for counterpropagating beams, i.e., in the limit of

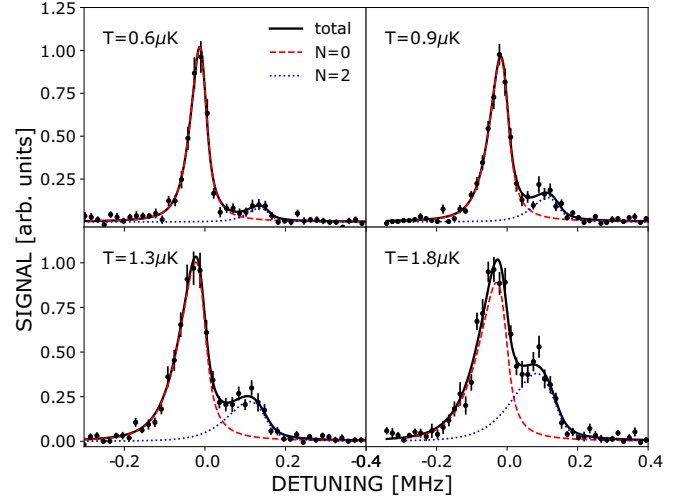


FIG. 1. Photoassociation spectra recorded when creating ground-state  $v = 0$   $^{86}\text{Sr } 5s29s \ ^1S_0$  ULRRM dimers using counterpropagating laser beams and the sample temperatures indicated. To emphasize the changes in spectral line shape that occur, the results in each panel are normalized to the same peak height. Fits obtained using the sum of contributions from just two states are included (see text). Note that the horizontal axis in this, and later, figures is expressed in units of frequency, i.e.,  $\omega/2\pi$ .

small  $\kappa$ , it is further approximated that  $j_\lambda(\kappa R_n / 2) \sim \delta_{\lambda,0} = \delta_{N,N'}$ . Sizable uncertainties in the fitted values, however, can result if the different contributions are not well resolved. As will be demonstrated, the excellent quality of the fits obtained using the predicted line shapes, i.e., Eq. (6), provides strong support for the present model.

#### IV. RESULTS AND DISCUSSION

Figure 1 shows photoassociation spectra recorded when creating  $^{86}\text{Sr } n = 29 \ ^1S_0$  dimers in the ground,  $v = 0$ , vibrational state using counterpropagating laser beams and a number of representative sample temperatures. To enable a more direct comparison of the spectral profiles, each data set is normalized to the same peak height. (As the sample temperature is reduced, however, the number of atoms remaining in the trap is reduced, resulting in lower signal levels.) As shown in Fig. 1, each measured spectrum can be well fit using Eq. (6) and the sum of contributions from just two product states whose separations,  $\Delta E$ , are observed to be essentially independent of sample temperature.

These observations point to the formation of just two different final molecular states. The energy separations,  $\Delta E$ , extracted from fitting the measured data are shown in Table I. Also included in Table I are the calculated values of  $\Delta E$  derived from the eigenenergies of the Rydberg dimer Hamiltonian together with those predicted by assuming the molecule behaves as a rigid rotor, in which event the rotational levels can be approximated by

$$E_{v,N} \simeq E_{v,N=0} + \frac{\hbar^2 N(N+1)}{2\mu R_n^2}, \quad (8)$$

TABLE I. Calculated and fitted level spacings for the transitions indicated. The asterisk denotes measurements using copropagating rather than counterpropagating laser beams. Column A shows rotational level spacings derived from the eigenenergies  $E_{v=0,N}$  of the  $^{86}\text{Sr}$  Rydberg dimer Hamiltonian. Column B lists the approximate values obtained when assuming the molecule behaves as a rigid rotor [Eq. (8)]. Columns C and D show level separations deduced from fits to measured  $^{86}\text{Sr}$  and  $^{84}\text{Sr}$  spectra, respectively, and represent the average of measurements taken at several different sample temperatures and trap operating conditions.

Rydberg		Level spacings (kHz)			
state	Levels	A	B	C	D
$5s29s\ ^1S_0$	$N = 0$ to $N = 2$	166	177	$167 \pm 12$	$173 \pm 12$
$5s30s\ ^1S_0$	$N = 0$ to $N = 2$	142	152	$140 \pm 11$	$141 \pm 11$
$5s31s\ ^1S_0$	$N = 0$ to $N = 2$	122	132	$127 \pm 10$	$123 \pm 10$
$5s32s\ ^1S_0$	$N = 0$ to $N = 2$	105	114	$106 \pm 9$	$113 \pm 9$
$5s33s\ ^1S_0$	$N = 0$ to $N = 2$	92	100	$94 \pm 8$	$92 \pm 8$
$5s29s\ ^1S_0^*$	$N = 0$ to $N = 1$	55	59	$54 \pm 7$	
	$N = 0$ to $N = 2$	166	177	$179 \pm 25$	

where  $R_n$  is the internuclear separation,  $\sim 1.8(n - \delta)^2 a_0$ , for the ground vibrational state. As seen in Table I, the separations in the calculated eigenenergies between the  $N = 0$  and  $N = 2$  levels are very similar to those seen in the experimental measurements, pointing to the creation of  $N = 0$  and  $N = 2$  rotational states. We note that the separation between the peaks in the photoassociation spectra that correspond to the production of  $N = 0$  and 2 states is typically smaller by an amount comparable to the thermal energy,  $k_B T \sim 20\text{--}40$  kHz, as compared to their actual energy separations (see Table I) due to the thermal averaging.

Figure 2 shows, for  $n = 29$ , the fractional contributions from  $N = 1$  and 2 states to the total dimer signal as a function of sample temperature when using co- and counterpropagating laser beams. Values derived from fits to the measured spectra, obtained by integrating their separate contributions to the total signal, are shown by symbols. The model predictions (lines) were calculated using the numerically integrated form factor [Eq. (1)]. The calculated fractional contributions from  $N = 2$  states increase steadily with sample temperature reflecting the fact that the contributions from  $N = 2$  partial waves increase with increasing collision energy in this temperature range [Eq. (2)].

For counterpropagating beams [Fig. 2(a)] the model predictions are in good agreement with the measured values. The small discrepancies seen at high temperatures for  $^{86}\text{Sr}$  may be partly due to the fitting error as the overlap between the  $N = 0$  and 2 features becomes larger. No significant production of  $N = 1$  states is predicted, or seen, consistent with the near-zero net photon momentum transfer.

Figure 3 compares photoassociation spectra recorded when creating  $n = 29$  to 31  $^{86}\text{Sr}$  dimers at a fixed sample temperature (1.3  $\mu\text{K}$ ). These data were recorded on a single day to ensure similar trap conditions and are normalized for small variations in trap density, laser powers, and the  $n$  dependence in the oscillator strengths for their creation [8]. As  $n$  decreases towards  $n = 25$  (for which  $R_n$  nearly matches  $a_s$ ), the overlap

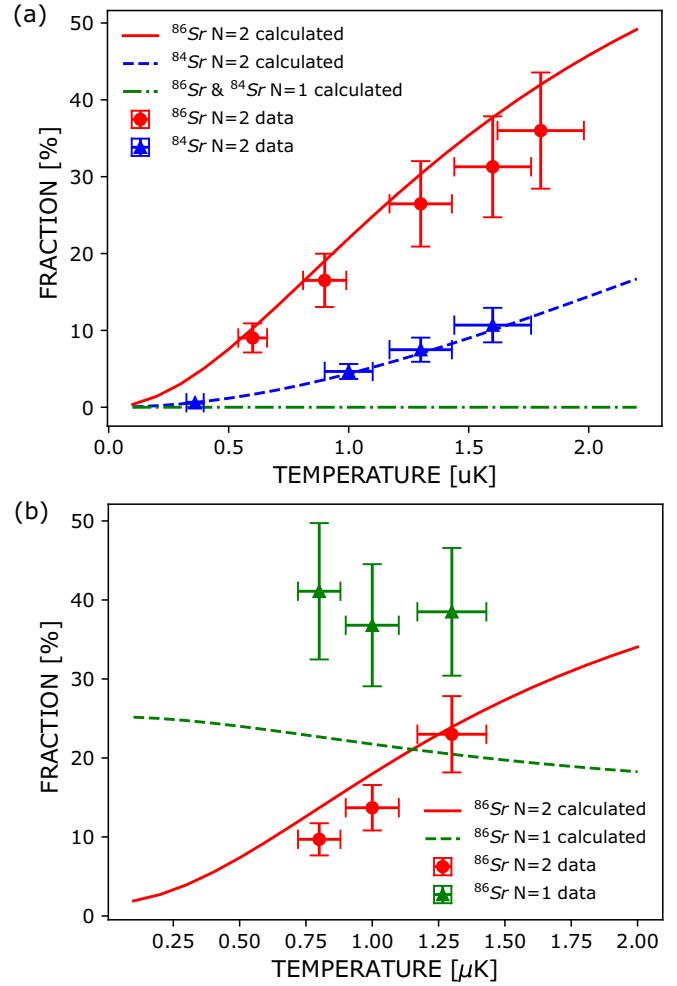


FIG. 2. Model predictions of the temperature dependence of the fractional contributions from  $N = 1$  and 2 states to the total  $\text{Sr } n = 29\ ^1S_0$  dimer signal for both (a) counter- and (b) copropagating laser beams. Panel (a) includes results for both  $^{84}\text{Sr}$  and  $^{86}\text{Sr}$  dimers and (b) results for only  $^{86}\text{Sr}$  dimers. Values obtained from fits to the experimentally measured spectra are also shown (symbols).

between the atomic scattering wave function and the ground-state molecular vibrational wave function decreases. Since for the present sample temperatures  $s$ -wave scattering typically dominates, this reduced overlap leads to a decrease in total dimer signal. As seen in Fig. 3, the (normalized) total dimer signal does decrease significantly as  $n$  decreases from  $n = 31$  to  $n = 29$ . (Experiment shows that the dimer signal continues to grow as  $n$  increases beyond 31.) Figure 3 also includes two-component fits to the data. The resulting level separations are included in Table I and are in very good agreement with the model predictions. As  $n$  increases, the separation between the rotational levels also decreases [ $\hbar^2 N(N + 1)/(2\mu R_n^2) \sim n^{-4}$ ] and for  $n \geq 34$  their associated features can no longer be reliably resolved. Note that, as the sample temperature rises, so too does the fractional contribution of  $N = 2$  states to the total dimer signal. Figure 4 shows the calculated fractional contribution from  $N = 2$  states as a function of  $n$  for a sample temperature of 1.3  $\mu\text{K}$  together with the fitted values, which are again in reasonable agreement with model predictions.

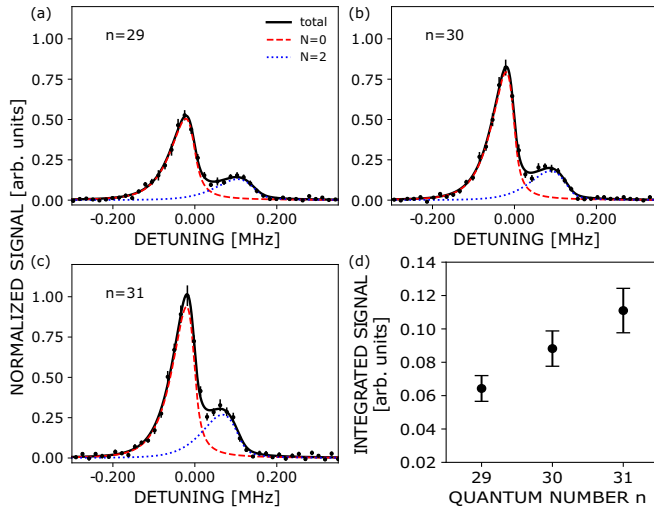


FIG. 3. (a)–(c) Photoassociation spectra recorded when creating ground-state  $v = 0$   $^{86}\text{Sr}$   $n = 29$  to  $31$   $^1S_0$  dimers using counterpropagating laser beams and a sample temperature of  $\sim 1.3$   $\mu\text{K}$ . The results are normalized for small changes in trap density, laser powers, and oscillator strengths. Fits obtained using the sum of contributions from just two states (see text) are also shown. (d)  $n$  dependence of the total dimer signal.

To further illustrate the importance of  $s$ -wave suppression in the case of  $^{86}\text{Sr}$  dimers, Fig. 5 shows photoassociation spectra recorded when creating  $^{84}\text{Sr}$  ULRRM dimers. For  $^{84}\text{Sr}$ , the  $s$ -wave atom-atom scattering length is small,  $a_s \sim 123a_0$ , and there is no node in the scattering wave function at the internuclear separations explored in the present work. In consequence, dimer production via the  $s$ -wave scattering channel is no longer suppressed. However, little change is expected in the higher-partial-wave channels between  $^{84}\text{Sr}$  and  $^{86}\text{Sr}$  due to the presence of a long-range centrifugal

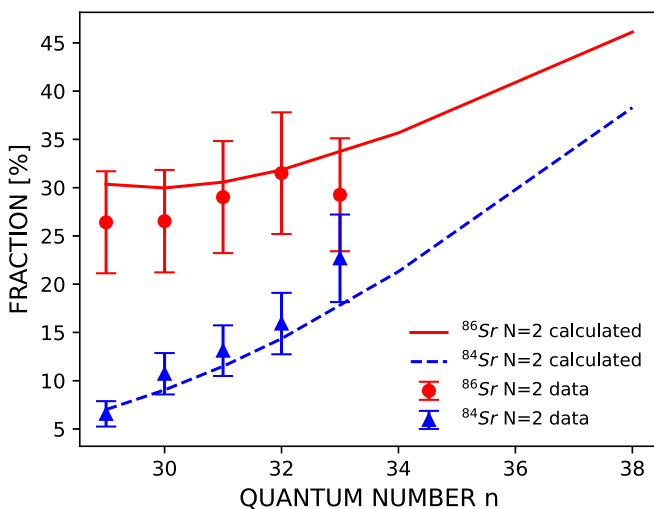


FIG. 4. Model predictions of the fractional contribution of  $N = 2$  states to the total dimer signal as a function of  $n$  for both  $^{84}\text{Sr}$  and  $^{86}\text{Sr}$  together with the results of experimental measurements. The results are for counterpropagating laser beams and a sample temperature of  $1.3$   $\mu\text{K}$ .

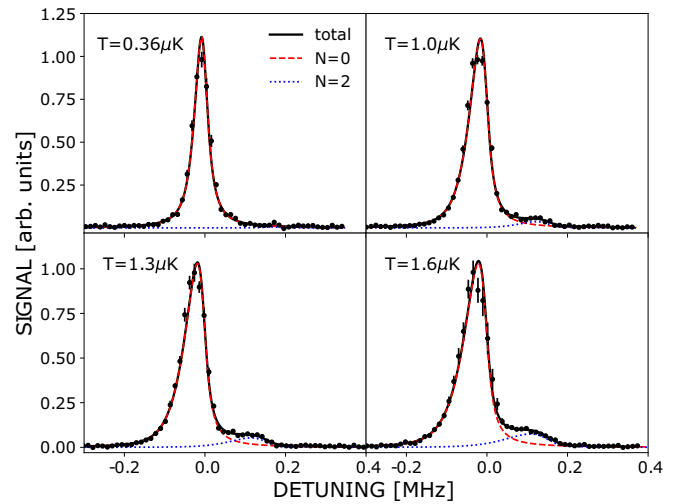


FIG. 5. Photoassociation spectra recorded when creating  $^{84}\text{Sr}$   $^1S_0$   $v = 0$   $5s29s$  dimers using counterpropagating laser beams and the sample temperatures indicated. Fits to the experimental data are also included. To emphasize the changes in the spectral profiles that occur, the results are normalized to the same peak height.

barrier. For  $^{84}\text{Sr}$ , therefore,  $s$ -wave scattering will be much stronger as compared to higher-partial-wave scattering. The measurements do, however, reveal a small contribution to the total  $^{84}\text{Sr}$  dimer signal at a detuning that is consistent with that for creation of  $N = 2$  states and that increases with sample temperature.

As seen in Fig. 4, measurements show that the fractional contribution of  $N = 2$  states to the total dimer signal also increases as  $n$  increases, behavior that is mirrored in the model predictions. The agreement between theory and experiment is again very good, further validating the present model by demonstrating it produces reliable predictions even when considering an atom pair with very different  $s$ -wave scattering characteristics.

Given that the trap operating conditions for  $^{84}\text{Sr}$  are rather different to those for  $^{86}\text{Sr}$ , it is difficult to normalize data sets obtained for each species to one another to compare their absolute relative dimer production rates. Nonetheless, attempts at such normalization suggest that, for  $n = 29$ , the dimer production rate for  $^{84}\text{Sr}$  is some 10 times larger than that for  $^{86}\text{Sr}$ . As  $n$  increases, however, this difference is seen to decrease due to the decreasing  $s$ -wave suppression for  $^{86}\text{Sr}$ .

Consider now the case of copropagating laser beams for which photon momentum transfer is maximized. Figure 6 shows photoassociation spectra recorded using copropagating laser beams when creating  $n = 29$   $^1S_0$  dimers. Whereas for counterpropagating beams Doppler broadening should be very small, that for copropagating beams will be significant, which is reflected in the increased widths of the spectral features. As a result the spectral features are less well resolved than for counterpropagating beams. Attempts to obtain a good fit to the measured spectra assuming contributions from just two product states with separations corresponding to that expected between the  $N = 0$  and  $N = 2$  levels proved unsuccessful. However, as demonstrated in Fig. 6, the spectra can be well fit by the sum of three separate contributions.

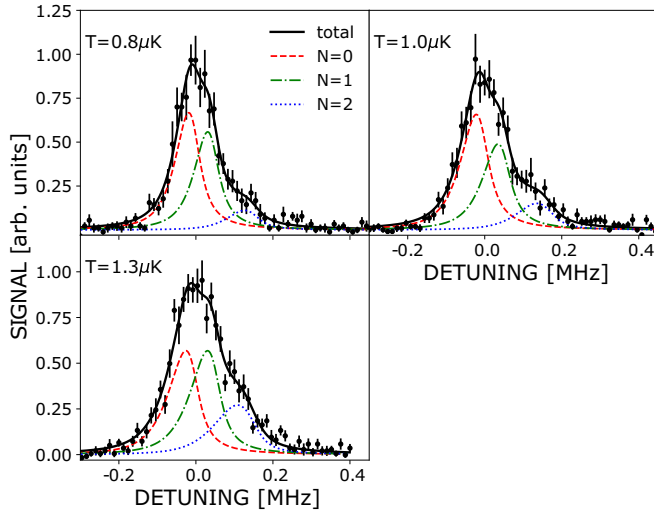


FIG. 6. Photoassociation spectra recorded when creating  $^{86}\text{Sr}$   $n = 29$   $^1S_0$  dimers using copropagating laser beams and the sample temperatures indicated. Also included are fits obtained using the sum of three states.

The separations between these three features are included in Table I and are consistent with those predicted between the  $N = 0$  and  $N = 1$  and 2 features, pointing to the formation of a mixture of all three.

Figure 2 includes the results of model simulations of the fractional contributions from the  $N = 1$  and 2 rotational levels for copropagating beams. The predicted fractions of  $N = 2$  states, which are reasonably well resolved, are in good agreement with experimental observations. The relative production of  $N = 1$  states inferred from the fits to the data, however, is somewhat higher than suggested by the model (see Fig. 2), which might be attributed to uncertainties introduced by the considerable overlap of the  $N = 0$  and  $N = 1$  features. Nonetheless, even though these features are not well resolved, the quality of the fits is such that the  $N = 1$  contribution and position (see Table I) are reasonably well determined. Clearly,  $N = 1$  states provide a sizable contribution to the dimer signal demonstrating that photon momentum transfer is very important in the creation of rotationally-excited dimers.

Earlier studies using  $n = 29$   $^3S_1$  dimers and copropagating laser beams (which results in the same total photon momentum transfer as for  $^1S_0$  dimers) suggested the additional production of  $N = 3$  dimers [15]. However, no evidence of their creation (at an expected detuning of  $\sim 350$  kHz) was seen in the present study of  $^1S_0$  dimers. Furthermore, the present model (see Fig. 2) does not predict the formation of significant numbers of such states. This suggests that the electron spin angular momentum might play a significant role in determining the final rotational distribution. However, direct coupling between the electron spin  $S$  and the rotational motion  $N$  is estimated to be negligible. Further work, therefore, will be required to examine any other mechanisms by which such spin to rotational angular momentum transfer might occur.

## V. CONCLUSIONS

The present measurements demonstrate the important roles played by atom-atom interactions, photon momentum transfer, and sample temperature in the production of rotationally excited ULRRMs and validate the model described in Sec. III which includes their effects. In future studies with  $^{86}\text{Sr}$  it will be interesting, for example, to see if similar rotational structure can be resolved when creating the less-well-localized vibrationally excited states, or even ground-state trimers, as well as exploring effects associated with reduced system mass by creating heteronuclear dimers in a two-component cold gas containing  $^{86}\text{Sr}$  and another alkali-metal or alkaline-earth element. In addition, direct comparisons to detailed measurements using  $^{86}\text{Sr}$   $n = 3$   $S_1$  dimers will help unravel the role played by spin angular momentum in determining the final distribution of rotational states.

## ACKNOWLEDGMENTS

This research has been supported by the National Science Foundation under Grants No. PHY-1904294 and No. PHY-2110596. The Vienna scientific cluster was used for the calculations.

- [1] J. P. Shaffer, S. T. Rittenhouse, and H. R. Sadeghpour, Ultracold Rydberg molecules, *Nat. Commun.* **9**, 1965 (2018).
- [2] C. Fey, F. Hummel, and P. Schmelcher, Ultralong-range Rydberg molecules, *Mol. Phys.* **118**, e1679401 (2020).
- [3] H. Saßmannshausen, J. Deiglmayr, and F. Merkt, Long-range Rydberg molecules, Rydberg macrodimers and Rydberg aggregates in an ultracold Cs gas, *Eur. Phys. J.: Spec. Top.* **225**, 2891 (2016).
- [4] C. Lippe, T. Eichert, O. Thomas, T. Niederprum, and H. Ott, Excitation of Rydberg molecules in ultracold quantum gases, *Phys. Status Solidi B* **256**, 1800654 (2019).
- [5] M. T. Eiles, Trilobites, butterflies, and other exotic specimens of long-range Rydberg molecules, *J. Phys. B: At., Mol., Opt. Phys.* **52**, 113001 (2019).
- [6] M. Schlagmüller, T. C. Liebisch, H. Nguyen, G. Lohead, F. Engel, F. Böttcher, K. M. Westphal, K. S. Kleinbach, R. Löw, S. Hofferberth, T. Pfau, J. Pérez-Ríos, and C. H. Greene, Probing an electron scattering resonance using Rydberg molecules within a dense and ultracold gas, *Phys. Rev. Lett.* **116**, 053001 (2016).
- [7] F. Engel, T. Dieterle, F. Hummel, C. Fey, P. Schmelcher, R. Löw, T. Pfau, and F. Meinert, Precision spectroscopy of negative-ion resonances in ultralong-range Rydberg molecules, *Phys. Rev. Lett.* **123**, 073003 (2019).
- [8] J. D. Whalen, S. K. Kanungo, R. Ding, M. Wagner, R. Schmidt, H. R. Sadeghpour, S. Yoshida, J. Burgdörfer, F. B. Dunning, and T. C. Killian, Probing nonlocal spatial correlations in quantum gases with ultra-long-range Rydberg molecules, *Phys. Rev. A* **100**, 011402(R) (2019).

- [9] S. K. Kanungo, Y. Lu, F. B. Dunning, S. Yoshida, J. Burgdörfer, and T. C. Killian, Measuring nonlocal three-body spatial correlations with Rydberg trimers in ultracold quantum gases, *Phys. Rev. A* **107**, 033322 (2023).
- [10] F. Camargo, R. Schmidt, J. D. Whalen, R. Ding, G. Woehl, S. Yoshida, J. Burgdörfer, F. B. Dunning, H. R. Sadeghpour, E. Demler, and T. C. Killian, Creation of Rydberg polarons in a Bose gas, *Phys. Rev. Lett.* **120**, 083401 (2018).
- [11] R. Schmidt, J. D. Whalen, R. Ding, F. Camargo, G. Woehl, S. Yoshida, J. Burgdörfer, F. B. Dunning, E. Demler, H. R. Sadeghpour, and T. C. Killian, Theory of excitation of Rydberg polarons in an atomic quantum gas, *Phys. Rev. A* **97**, 022707 (2018).
- [12] J. Tempere, W. Casteels, M. K. Oberthaler, S. Knoop, E. Timmermans, and J. T. Devreese, Feynman path-integral treatment of the BEC-impurity polaron, *Phys. Rev. B* **80**, 184504 (2009).
- [13] T. Scheuing and J. Pérez-Ríos, Quasi-static lineshape theory for Rydberg excitations in high-density media, *Atoms* **11**, 95 (2023).
- [14] O. Thomas, C. Lippe, T. Eichert, and H. Ott, Photoassociation of rotating ultra-long range Rydberg molecules, *J. Phys. B: At., Mol., Opt. Phys.* **51**, 155201 (2018).
- [15] Y. Lu, J. D. Whalen, S. K. Kanungo, T. C. Killian, F. B. Dunning, S. Yoshida, and J. Burgdörfer, Resolving rotationally excited states of ultralong-range Rydberg molecules, *Phys. Rev. A* **106**, 022809 (2022).
- [16] S. Stellmer, F. Schreck, and T. C. Killian, *Annual Review of Cold Atoms and Molecules* (World Scientific, Singapore, 2014), Chap. 1.
- [17] Y. N. Martinez de Escobar, P. G. Mickelson, M. Yan, B. J. DeSalvo, S. B. Nagel, and T. C. Killian, Bose-Einstein condensation of  $^{84}\text{Sr}$ , *Phys. Rev. Lett.* **103**, 200402 (2009).
- [18] B. J. DeSalvo, J. A. Aman, F. B. Dunning, T. C. Killian, H. R. Sadeghpour, S. Yoshida, and J. Burgdörfer, Ultra-long-range Rydberg molecules in a divalent atomic system, *Phys. Rev. A* **92**, 031403(R) (2015).
- [19] *Rydberg States of Atoms and Molecules*, edited by R. F. Stebbings and F. B. Dunning (Cambridge University Press, Cambridge, UK, 1983).
- [20] T. F. Gallagher, *Rydberg Atoms* (Cambridge University Press, Cambridge, UK, 1994).
- [21] K. M. Jones, P. D. Lett, E. Tiesinga, and P. S. Julienne, Fitting line shapes in photoassociation spectroscopy of ultracold atoms: A useful approximation, *Phys. Rev. A* **61**, 012501 (1999).